analytical chemistry

pubs.acs.org/ac Article

Periodic Photobleaching with Structured Illumination for Diffusion Imaging

Ziyi Cao, Dustin M. Harmon, Ruochen Yang, Aleksandr Razumtcev, Minghe Li, Mark S. Carlsen, Andreas C. Geiger, Dmitry Zemlyanov, Alex M. Sherman, Nita Takanti, Jiayue Rong, Yechan Hwang, Lynne S. Taylor, and Garth J. Simpson*

Cite This: *Anal. Chem.* 2023, 95, 2192–2202 Read Online

ACCESS | Metrics & More | Article Recommendations | Supporting Information

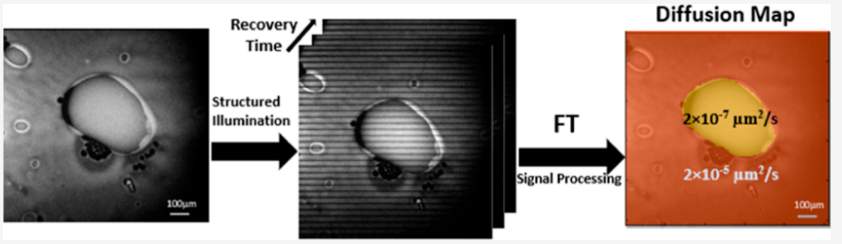

ABSTRACT: The use of periodically structured illumination coupled with spatial Fourier-transform fluorescence recovery after photobleaching (FT-FRAP) was shown to support diffusivity mapping within segmented domains of arbitrary shape. Periodic "comb-bleach" patterning of the excitation beam during photobleaching encoded spatial maps of diffusion onto harmonic peaks in the spatial Fourier transform. Diffusion manifests as a simple exponential decay of a given harmonic, improving the signal to noise ratio and simplifying mathematical analysis. Image segmentation prior to Fourier transformation was shown to support pooling for signal to noise enhancement for regions of arbitrary shape expected to exhibit similar diffusivity within a domain. Following proof-of-concept analyses based on simulations with known ground-truth maps, diffusion imaging by FT-FRAP was used to map spatially-resolved diffusion differences within phase-separated domains of model amorphous solid dispersion spin-cast thin films. Notably, multi-harmonic analysis by FT-FRAP was able to definitively discriminate and quantify the roles of internal diffusion and exchange to higher mobility interfacial layers in modeling the recovery kinetics within thin amorphous/amorphous phase-separated domains, with interfacial diffusion playing a critical role in recovery. These results have direct implications for the design of amorphous systems for stable storage and efficacious delivery of therapeutic molecules.

INTRODUCTION

Low aqueous solubility, common to many small molecule active pharmaceutical ingredients (APIs), has the potential to negatively impact bioavailability.[1] One widespread method of addressing these thermodynamic limitations is through kinetics, in which the API is prepared by molecular dispersion in a glassy amorphous polymer matrix rather than in a crystalline state.[2,3] Such amorphous solid dispersions (ASDs) are typically metastable, with shelf-life and dissolution rates controlled kinetically through restricted API mobility within the glassy polymer matrix. Formation of crystalline or amorphous phase separations arising during storage or during dissolution have the potential to greatly slow dissolution kinetics, with corresponding reductions in bioavailability. As such, methods for characterizing phase stability and mobility of APIs within ASD formulations can provide insights into mechanisms contributing to losses in bioavailability.

Previously, THz spectroscopy and NMR have been employed to probe fast rotational or local motion. Buron et al. reported graphene mobility mapping with THz spectroscopy,[4] and Williams et al. reported ^{19}F NMR measurements of the rotational mobility of proteins.[5] However, rotational and vibrational motions may not directly correlate with translational motions driving mass transport necessary for phase separation and/or crystallization. Despite the clear benefits, few techniques for direct measurements of translational diffusion have been demonstrated. Two practical limitations complicate translational diffusion measurements in ASD assemblies: (i) the glacial pace of molecular motion within many ASD matrices, requiring measurements over small distances and long times, and (ii) structural heterogeneity (particularly following phase separation), such that ensemble-averaged measurements routinely do not reflect the variance in

Received: July 8, 2022
Accepted: December 28, 2022
Published: January 19, 2023

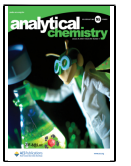

local environments most important for nucleation and growth of phase-transformed domains.

One experimentally simple approach to perform local diffusion analysis over short (<500 nm) distances is fluorescence recovery after photobleaching (FRAP), which is commonly used in molecular mobility analysis in cellular biology, soft materials science, and polymer science.[6,7] In FRAP, native or doped fluorescence within a targeted region of a sample is photobleached by focused excitation. If the sample exhibits translational diffusive mobility, the photobleached molecules and the fluorescent molecules will exchange, producing fluorescence recovery within the photobleached region. Characteristic timescales for this recovery can inform mathematical models of diffusion.[8] FRAP was first demonstrated by Peters et al. in 1974 to measure the diffusion of membrane proteins in red blood cell ghosts.[9] More recently, FRAP has been used to detect protein aggregation during liquid−liquid phase separation,[10] to characterize the impact of structure on solute diffusivity in microporous tissue engineering scaffolds,[11] to compare the mobility of 45 proteins involved in synaptic transmission, and to measure diffusion anisotropy in porcine ligaments.[12]

FRAP is typically performed by photobleaching a single localized punctum, yielding a high signal to noise ratio (SNR) bleach point-spread function (PSF) and fast recovery to minimize $1/f$ noise. However, single point-bleach approaches suffer from several limitations. First and most obviously, point-photobleach measurements only inform on the diffusivity in the region immediately adjacent to the photobleach spot,[13] introducing measurement bias in heterogeneous samples exhibiting significant spatial variance in the diffusivity across the field of view (FoV) such as expected within phase-separated ASD domains. Second, analysis of the subsequent recovery can be highly sensitive to the shape of the PSF defining the original photobleach profile. Changes in the PSF from astigmatism or from out-of-focus photobleaching can substantially change both the overall timescale for FRAP recovery and the accuracy with which the diffusion coefficient can be recovered.[14] Third, point-bleach FRAP is generally insensitive to discrimination between normal versus anomalous diffusion.[15] Fourth, multi-photon excited FRAP can be particularly challenging for point-bleach methods due to local heating; parking the excitation beam at one location long enough to induce substantial photobleaching often results in heat deposition rates from weak but nonzero one-photon absorption exceeding heat dissipation, with corresponding rapid increases in local temperature.[16] Finally, the total integrated photobleach power in point-bleach FRAP is ultimately limited by saturation. High photobleaching powers can introduce nonlinearities in the PSF (e.g., top−hat profile from saturation), resulting in intensity-dependent PSFs that can exacerbate challenges in quantification from uncertainties in the PSF.[17]

Several alternative photobleaching patterns have been proposed to circumvent these limitations. Multiple, single point FRAP measurements have been performed in parallel to measure diffusion in several discrete regions of a sample.[18,19] This was achieved with a confocal beam-scanning microscope by programming an acousto-optical modulator (AOM) or acousto-optical tunable filter to rapidly modulate laser power while scanning, producing multiple photobleached regions in the field-of-view.[20] Hagen and co-workers developed a FRAP technique that simultaneously performs an arbitrary number of single-point FRAP experiments across a FoV using structured illumination in a programmable array microscope (PAM).[21] The PAM uses a spatial light modulator as a photobleaching mask to produce multiple photobleached spots at the sample plane. The authors used this technique to measure local variation in diffusion for erbB3 (HER3) receptor tyrosine kinase in cells. Alternative (non-point) photobleaching patterns have also allowed FRAP measurements of larger areas of arbitrary shape.[22−27] However, this collective set of studies implicitly assume that the diffusion recorded at a small number of select locations can accurately inform on the diffusivity in adjacent regions. As the complexity and heterogeneity of samples increases, the number of systems for which this assumption is likely to fail will correspondingly increase.

To enable mobility analysis within heterogeneous media, several strategies have been considered for recovery of full spatially-resolved diffusion maps, in which the diffusion coefficient is independently recovered in each pixel or domain in an image. Superfine and co-workers leveraged selective plane illumination to photobleach an entire two-dimensional slice through a sample and generate a fluorescence recovery image of NLS-GFP and 53BP1-mCherry in live cells.[28] The authors used a combination of a cylindrical lens and an annulus to produce a line Bessel sheet for photobleaching the YZ plane. Horizontal imaging of the fluorescence recovery was achieved using a right-angle reflective prism.[29] A simple closed-form solution to the diffusion equation was not possible in this case due to the complexity of the illumination profile. Instead, the investigators used a diffusion simulation to convert from fluorescence recovery time to diffusion coefficient. While an impressive tour de force, the work by Superfine and co-workers requires a light-sheet approach not commonly available in most laboratory microscopes nor easy to retrofit.

The ability to map local diffusivity is particularly important in the analysis of ASDs, in which water exposure has been shown to induce phase separation. Prior studies by Taylor and co-workers suggest a critical role for amorphous/amorphous phase separation within ASDs, which can profoundly impact dissolution kinetics.[30] Infrared spectroscopy studies suggest sensitivity of moisture-induced amorphous−amorphous phase separation on drug−polymer interaction strength, ASD hygroscopicity, and API water affinity.[30,31] At relatively high drug loadings, dramatic reductions in API dissolution kinetics were observed, together with an observed increase in the rate of polymer dissolution relative to that of the API.[32] Fluorescence microscopy using a hydrophobic-sensitive Nile red fluorescent dye was used to observe formation of phase-separated domains in hydrated matrices of ASDs following storage at high humidity and during dissolution.[33] The observation of phase-separated API-rich domains at high drug loading provides a possible explanation for the "falling-off-a-cliff" behavior in dissolution kinetics, in which dissolution rates are driven by dissolution of the amorphous drug-rich phase-separated regions which form a barrier layer at the ASD-solvent interface, rather than the polymer matrix. Improved predictive modeling of dissolution kinetics within ASD systems prone to phase separation requires methods capable of probing molecular mobility within these microscopic phase-separated domains.

In this work, we demonstrate an alternative computational imaging approach for full spatial mapping of molecular diffusivity within heterogeneous media based on periodically

https://doi.org/10.1021/acs.analchem.2c02950
Anal. Chem. 2023, 95, 2192−2202

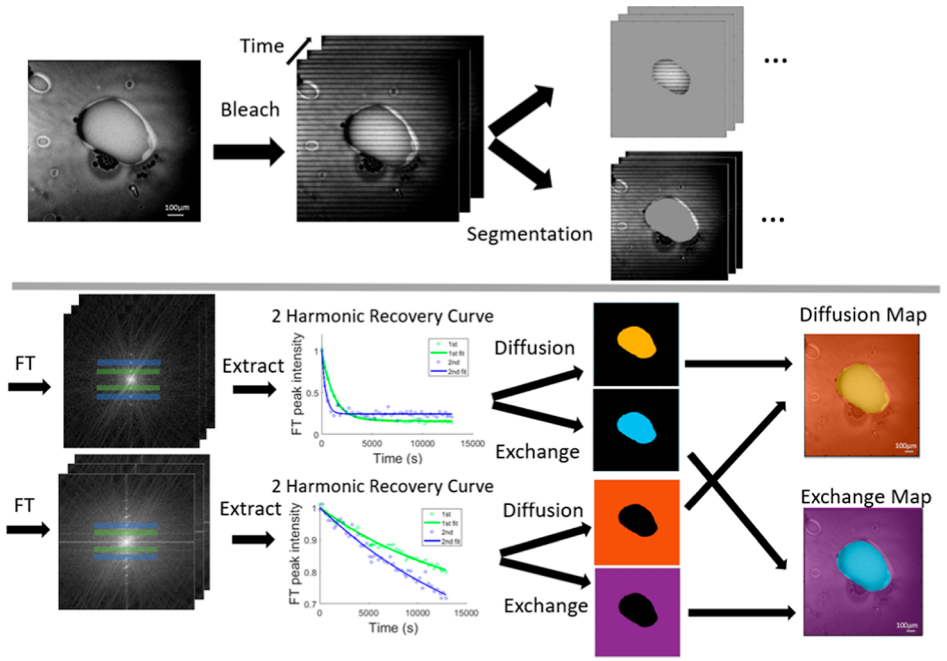

Figure 1. Graphical depiction of diffusion mapping by FT-FRAP. Following periodically structured photobleaching (top middle), image stacks corresponding to recovery within segmented domains (top right) are compiled and Fourier-transformed (bottom-left), producing a series of peaks in the spatial frequency domain. Mobility was extracted by integrating the area of the harmonic peaks over time, followed by least-squares fitting to single exponential decays (bottom-middle). Recovery curves from multiple harmonics were combined to decompose into diffusion and exchange contributions and compiled to generate spatially resolved diffusion/exchange maps (bottom-right) for multiple segments.

patterned illumination followed by Fourier transform manipulations to isolate the dynamic components of the image stack. Using Fourier transform FRAP (FT-FRAP), a diffusion coefficient can, in principle, be independently recovered at every pixel within the FoV. In FT-FRAP, a fluorescent sample is photobleached using patterned illumination to produce a periodic fluorescent pattern. As shown in Figure 1, the FRAP signal spread over the entire FoV in real-space is concentrated to a set of sharp puncta in the spatial frequency domain through Fourier transformation, with each peak representing a spatial frequency harmonic of the photobleach pattern. Image segmentation enables simultaneous diffusion analysis within multiple arbitrarily-shaped domains. A key advantage of FT-FRAP is direct compatibility with conventional beam-scanning microscopy instrumentation used in multi-photon and confocal microscopy, potentially facilitating widespread adoption. Following proof of concept studies with computational models, FT-FRAP is applied to studies of molecular mobility within model ASD thin films, providing information in multi-harmonic analysis not easily recoverable by conventional point-bleach FRAP measurements.

THEORY

Normal 2D Diffusion in a Homogeneous Assembly. Normal diffusion can be described by Fick's Law of Diffusion, as shown in eq 1, in which $C(\boldsymbol{\rho},t)$ is the concentration distribution of the analyte of interest as a function of position $\boldsymbol{\rho}$ and time t, and $\mathbf{D}$ is the three-dimensional diffusion tensor

$$\frac{\partial}{\partial t}C(\boldsymbol{\rho}, t) = \nabla \mathbf{D} \nabla C(\boldsymbol{\rho}, t) \tag{1}$$

Equation 1 is arguably simpler to solve in the spatial Fourier transform domain, in which the gradient operations transform as products with diagonal functions. The outcome is shown in eq 2, in which $\tilde{C}$ is the spatial Fourier transform of C and $\overline{\boldsymbol{\nu}}$ is the 3D spatial wavevector.

$$\frac{\partial}{\partial t}\tilde{C}(\overline{\boldsymbol{\nu}}, t) = -4\pi^2 \overline{\boldsymbol{\nu}}^{\mathrm{T}} D \overline{\boldsymbol{\nu}} \tilde{C}(\overline{\boldsymbol{\nu}}, t) \tag{2}$$

In the case of isotropic diffusion in the (x,y) plane, the diffusion tensor $\mathbf{D}$ can be replaced by a scalar diffusion coefficient D, such that the two-dimensional solution to eq 2 is given by eq 3.

$$\frac{\partial}{\partial t}\tilde{C}(\overline{\boldsymbol{\nu}}, t) = -4\pi^2(\overline{\nu}_x^2 + \overline{\nu}_y^2) D \tilde{C}(\overline{\boldsymbol{\nu}}, t) \tag{3}$$

In the spatial frequency domain, this differential equation has the form $A' = kA$, the general solution to which is $A(t) = a\, \mathrm{e}^{-k_1 t} + b\, \mathrm{e}^{k_2 t}$. Imposing boundary conditions consistent with a temporal decay along a concentration gradient yields a simple exponential decay in the spatial frequency domain.

$$\tilde{C}(\overline{\nu}_x, \overline{\nu}_y, \mathrm{t}) = \tilde{C}(\overline{\nu}_x, \overline{\nu}_y, 0)\mathrm{e}^{-4\pi^2(\overline{\nu}_x^2 + \overline{\nu}_y^2)Dt} \tag{4}$$

For a given point in the spatial frequency $(\overline{\nu}_x, \overline{\nu}_y)$, the time-dependent amplitude decays exponentially with a decay constant dependent only on D and $(\overline{\nu}_x, \overline{\nu}_y)$ and is independent of the initial distribution $\tilde{C}(\overline{\nu}_x, \overline{\nu}_y, 0)$.

Periodically Patterned Illumination in FT-FRAP. The concise mathematical form to the solution for normal diffusion given in eq 4 enables simplified analysis of FRAP experiments in the spatial frequency domain. To take full advantage of this capacity, photobleach patterns were designed to concentrate the FRAP signal to a handful of discrete spatial frequencies. As described in prior work,[15] the comb patterns used in this study were generated by a series of evenly spaced photobleached

https://doi.org/10.1021/acs.analchem.2c02950
Anal. Chem. 2023, 95, 2192−2202

stripes (see Figure 1, top left). In the spatial frequency domain, the comb pattern transforms as a series of evenly spaced impulses (see Figure 1, bottom left), concentrating the integrated bleach power in the real-space image to localized puncta of high SNR in the spatial FT domain.

Patterned photobleaching can be described by eq 5, where $\boldsymbol{\rho}$ is position, $C(\boldsymbol{\rho},0)$ is the initial post-bleach image, $C_0(\boldsymbol{\rho})$ is the pre-bleach image, and $C_b(\boldsymbol{\rho})$ is the photobleach pattern.

$$C(\boldsymbol{\rho}, 0) = C_0(\boldsymbol{\rho}) \cdot C_b(\boldsymbol{\rho}) \tag{5}$$

The photobleach pattern, $C_b(\boldsymbol{\rho})$, can itself be described as the convolution of a comb function with the point spread function (PSF) of the laser beam, as shown in eq 6.

$$C_b(\boldsymbol{\rho}) = \text{comb}(\boldsymbol{\rho}) \otimes \text{PSF}(\boldsymbol{\rho}) \tag{6}$$

Peak Shape Analysis in the Frequency Domain. Two-dimensional spatial Fourier transformation of eq 5 yields eq 7,

$$\tilde{C}(\bar{\nu}, 0) = \tilde{C}_0(\bar{\nu}) \otimes \left(\text{FT of comb photobleach} \bullet \text{FT of PSF} \right) \tag{7}$$

where $\tilde{C}(\bar{\nu}, 0)$ is the FT of the initial post-bleach, and $\tilde{C}_0(\bar{\nu})$ is the FT of the pre-bleach image. Note that the convolution operation depicted in eq 6 with $C_b(\boldsymbol{\rho})$ transforms to the multiplication of FT of the two functions depicted in eq 7. Similarly, the multiplication in eq 5 becomes a convolution following Fourier transformation.

If $C_0(\boldsymbol{\rho})$ from eq 5 is a constant, as expected for a homogeneous sample, then $\tilde{C}_0(\bar{\nu})$ is an impulse and convolution by $\tilde{C}_0(\bar{\nu})$ simply recovers the impulse series inside the parentheses of eq 7, the amplitudes of which are dictated by the FT of the photobleach point spread function. However, if $C_0(\boldsymbol{\rho})$ exhibits structure, then $\tilde{C}_0(\bar{\nu})$ will be convolved with each peak from the FT of the comb photobleach. This operation will produce a series of peaks that contain information about the spatial contrast in $C_0(\boldsymbol{\rho})$, each scaled by the corresponding spatially modulated FRAP amplitude. This relationship is captured in eq 8, where n is the harmonic, A_n is an amplitude scaling based on the FT of the PSF in eq 7, and the equation assumes a comb photobleach pattern in the x axis.

$$\tilde{C}_0(\bar{\nu}_x - n\bar{\nu}_0, \bar{\nu}_y) \cong \tilde{C}_0(\bar{\nu}_x, \bar{\nu}_y) A_n \tag{8}$$

The harmonic peaks at $n\bar{\nu}_0$, where $\bar{\nu}_0$ is the fundamental frequency, in theory have an identical relative peak shape which contains information about the structure of the image. This equation only holds for low frequency features where $\bar{\nu}_x < \bar{\nu}_0/2$ to ensure no overlap between peaks in the spatial frequency domain. This description at $t = 0$ provides a foundation for interpreting the time-evolution within given spatial domains, considered in the next section.

Image Segmentation and Time-Dependent Analysis. Before bringing in the time-dependence, we will assume that the initial post-bleach image $C_0(\boldsymbol{\rho})$ contains segmented domains of local, isotropic diffusion with diffusion coefficient D_i in each domain, i, as shown in eqs 9 and 10.

$$C_0(\boldsymbol{\rho})_{\text{tot}} = \sum_i C_0(\boldsymbol{\rho})_i \tag{9}$$

$$\tilde{C}_0(\bar{\nu})_{\text{tot}} = \sum_i \tilde{C}_0(\bar{\nu})_i \tag{10}$$

The solution in eq 4 holds for each domain, such that the contributions from the sum of isolated domains produce the following time-evolving peak shape about $n\bar{\nu}_0$

$$\tilde{C}(\bar{\nu}_x - n\bar{\nu}_0, \bar{\nu}_y, t) = \sum_i \tilde{C}_0(\bar{\nu}_x - n\bar{\nu}_0, \bar{\nu}_y, 0)_i \, e^{-4\pi^2 (n\bar{\nu}_0)^2 D_i t} \tag{11}$$

From eq 11, analysis in the FT domain produces simple exponential decays for the time-dependent evolution of the amplitudes within each isolated segmented region, each of which decays with a unique temporal decay constant related to the local diffusion coefficient and the spatial harmonic n.

Diffusion Modeling. The system under investigation consists of phase-separated domains formed upon water vapor exposure of a homogeneous mixture of ritonavir and biocompatible polymer. Following water vapor exposure, previous studies have shown that ritonavir-enhanced and ritonavir-depleted phases dissociate to form domains of spatially varying molecular mobility.[33] The kinetics of mobility within this two-phase system can depend sensitively on the relative diffusivity within the two domains and the 3D microscopic architecture of the interfacial layered structure. Several different physical models for mobility within and between the phase-separated domains were considered, illustrations of which are provided in Figure 2.

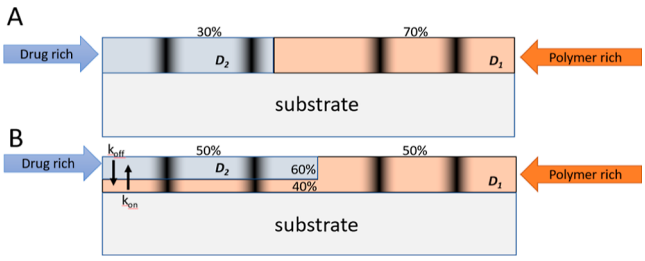

Figure 2. Physical cross-sectional models considered for molecular mobility within phase-separated domains in spin-cast ASD films: (A) monolithic domains, contacting only at the lateral interfaces, (B) hydrophilic sublayer, consisting of a thin polymer-rich interfacial layer at the hydrophilic glass interface.

(i) Monolithic domains. In the first and simplest model shown in Figure 2A, it is assumed that each phase-separated domain extends monolithically from the air-exposed interface through to the substrate, with exchange between the phase-separated domains arising only at the lateral interfaces between domains. In this model, mobility within each isolated domain is described diffusively, but with a unique diffusion coefficient for each isolated phase. Deviations from normal diffusivity can be attributed to anomalous diffusion within the bulk materials. The kinetic model for monolithic domains is relatively straightforward to describe mathematically.

Anomalous diffusion is defined as diffusion that deviates from normal Brownian diffusion. Under the continuous-time random walk model described by Metzler and Klafter,[34] and used in this study and a previous study,[15] anomalous diffusion can deviate from normal diffusion in two ways: a deviation in the characteristic wait time (characterized by the parameter α) and/or a deviation in the distribution of step lengths-(characterized by the parameter μ). The two-dimensional

https://doi.org/10.1021/acs.analchem.2c02950
Anal. Chem. 2023, 95, 2192−2202

solution to the diffusion equation for isotropic anomalous diffusion in the spatial frequency domain is given by eq 12, where E_α is the Mittag−Leffler function, which is a fractional generalization of an exponential function ($E_1(x) = e^x$).

$$\tilde{C}(\overline{\nu}_x, \overline{\nu}_y, t) = \tilde{C}(\overline{\nu}_x, \overline{\nu}_y, 0)E_\alpha(-(2\pi\sqrt{\overline{\nu}_x^2 + \overline{\nu}_y^2})^\mu Dt^{2\alpha/\mu}, \alpha) \tag{12}$$

Note that when $\alpha = 1$ and $\mu = 2$, eq 12 simplifies to eq 4, which is the solution for normal diffusion.

Assuming the recovery kinetics within each domain can be modeled as constant within a domain (consistent with a negligible perturbation by lateral exchange), segmentation of the domains followed by recovery analysis using either eqs 11 or 12 should allow unique determination of the diffusion coefficient within a given segmented domain.

(ii) Interfacial Diffusion (Figure 2B). Given the hydrophilic nature of the glass substrate, it is plausible that the hydrophilic polymer-rich domain may extend to form the initial contact with the substrate, producing a thin intermediate layer between the substrate and the hydrophobic ritonavir-rich domains depicted in Figure 2B. In this model, vertical (normal to the interface) exchange between the hydrophilic and hydrophobic phase-separated domains may arise at all locations exhibiting hydrophobic domains. Deviations from normal diffusion can arise in such a model through kinetic exchange of material across the hydrophilic/hydrophobic interface. In such cases, the kinetics of the exchange process can be integrated into the model using a desorption/adsorption mechanism. If the two contacting domains exhibit a substantial difference in diffusivity, the rate-limiting step in recovery may be desorption from the highly viscous hydrophobic domain to the hydrophilic layer with higher lateral mobility.

In this diffusion + exchange kinetic model, analysis in the Fourier domain offers distinct practical advantages for combining diffusion and exchange, as both are described by exponential processes in the spatial frequency domain (but not in real-space), with scalar exchange rate constants given by k_{off} for desorption from the API-rich domain to the mobile polymer layer and k_{on} for adsorption back to the API-rich domain. For a given spatial frequency, the kinetics of recovery for a domain containing both hydrophilic and hydrophobic layers in intimate vertical contact can be described by the following kinetic equations by extension of the expression written for diffusion alone in eq 11, with $\tilde{A}$ representing the amplitude of the n-th harmonic Fourier peak arising from the API-rich amorphous layer and $\tilde{P}$ the corresponding amplitude from the polymer-rich (hydrophilic) layer within an amorphous phase-separated domain.

$$\frac{\partial}{\partial t}\tilde{A} = 4\pi^2 n^2 \overline{\nu}_0^2 D_A \tilde{A} - k_{off}\tilde{A} + k_{on}\tilde{P} \tag{13}$$

$$\frac{\partial}{\partial t}\tilde{P} = k_{off}\tilde{A} - 4\pi^2 n^2 \overline{\nu}_0^2 D_A \tilde{P} - k_{on}\tilde{P} \tag{14}$$

The paired set of differential equations in eqs 13 and 14 can be written in the matrix form

$$\frac{\partial}{\partial t}\begin{bmatrix}\tilde{A}_n \\ \tilde{P}_n\end{bmatrix} = \begin{bmatrix}-4\pi^2 n^2 \overline{\nu}_0^2 D_A - k_{off} & k_{on} \\ k_{off} & -4\pi^2 n^2 \overline{\nu}_0^2 D_P - k_{on}\end{bmatrix}\begin{bmatrix}\tilde{A}_n \\ \tilde{P}_n\end{bmatrix} \tag{15}$$

Since all effects in the kinetic model appear as first order in the spatial Fourier transform domain, matrix methods for coupled first-order kinetics provide a straightforward route for numerical evaluation of the coupled differential equations. The matrix expression in eq 15 can be written in matrix/vector notation as follows

$$\frac{\partial}{\partial t}\mathbf{a} = \mathbf{K}\mathbf{a} \tag{16}$$

One can define a time-dependent transformation matrix $\mathbf{P}$ given by the orthonormal eigenvectors of $\mathbf{K}$, such that $\mathbf{a}=\mathbf{P}\mathbf{b}$. Substitution yields the following expression.

$$\frac{\partial}{\partial t}\mathbf{P}\mathbf{b} = \mathbf{K}\mathbf{P}\mathbf{b} \tag{17}$$

Left-multiplication by $\mathbf{P}^{-1}$ yields the following expression, bearing in mind that $\mathbf{P}^{-1}\mathbf{P} = \mathrm{I}$ for an orthonormal matrix.

$$\frac{\partial}{\partial t}\mathbf{b} = \mathbf{P}^{-1}\mathbf{K}\mathbf{P}\mathbf{b} = \Lambda\mathbf{b} \tag{18}$$

In eq 18, the matrix Λ consists of a diagonal matrix of eigenvalues for the matrix $\mathbf{K}$. Each row of eq 18 is of the form $b_i' = \lambda b_i$, with a corresponding solution of $b_i(t) = e^{\lambda t}b_i(0)$. The collective results can be expressed in the following shorthand notation, in which each diagonal element of the matrix Λ is placed in the exponential and multiplied by time.

$$\mathbf{b}(t) = e^{\Lambda t}\mathbf{b}(0) \tag{19}$$

Substituting $\mathbf{a} = \mathbf{P}\mathbf{b}$ allows the expression to be recast in terms of the original concentrations of a

$$\mathbf{a}(t) = \mathbf{P}\mathbf{b}(t) = \mathbf{P}\, e^{\Lambda t}\mathbf{b}(0) = \mathbf{P}\, e^{\Lambda t}\mathbf{P}^{-1}\mathbf{a}(0) \tag{20}$$

It is useful to explore several key limits in the general expression given by eq 20. Most notably, the limit of negligibly small values of $\tilde{P}_n$ is worthwhile to consider for two key reasons: (i) the fluorophores investigated exhibit preferential partitioning in the hydrophobic domains, and (ii) relatively fast diffusion within the polymer domains corresponds to fast decay of all harmonic peaks for $n > 0$, such that long-time kinetics will be dominated by $\tilde{A}_n$. In the limit of $\tilde{P}_n \to 0$, the expression for the time-dependence of the harmonic peaks is remarkably straightforward to evaluate from eq 20.

$$\tilde{A}_n(t) \cong \tilde{A}_n(0)e^{-(4\pi^2 n^2 \overline{\nu}_0^2 D_A + k_{off})t} \tag{21}$$

Details are provided in the Supporting Information on the subsequent matrix representations and inversion operations to recover the maximum likelihood estimates for the diffusion and exchange coefficients and the corresponding uncertainties from the fits.

MATERIALS AND METHODS

Poly(vinylpyrrolidone-*co*-vinyl acetate) (PVPVA) (Kollidon VA 64) was supplied by the BASF Corporation (Ludwigshafen, Germany). Ritonavir was purchased from ChemShuttle

https://doi.org/10.1021/acs.analchem.2c02950
Anal. Chem. 2023, 95, 2192−2202

(Jiangsu, China). Nile red was purchased from Sigma-Aldrich (St. Louis, MO).

Thin films of ASD or each component were prepared by spin coating using a KW-4A spin-coater (Chemat Scientific, Northridge CA). Stock solutions of each component or ASD were prepared in methanol with 10% w/v solid content by dissolving the desired ratio of each component. An aliquot of stock solution (100 μL) was placed on a cover glass (#1.5 thickness) and spin coated at 1000 rpm for 10 s, followed by 3000 rpm for 45 s.

Phase-separated films were prepared by subsequent exposure to high (100%) relative humidity (RH) in an enclosed chamber containing distilled water at 37 °C for 12 h to induce phase separation. Films were then dried in a vacuum oven overnight before performing measurements.

To conduct FT-FRAP analysis, the dried film samples were first transferred into a controlled environment for in situ stability testing (CEIST) system, described in detail previously.[37] RH of 97 ± 1% and ambient temperature of 20 ± 1 °C were maintained for all experiments through shared head-space with a vapor equilibrated with saturated potassium sulfate aqueous solution.

A schematic of the one-photon excited microscope used in this study for comb photobleach FT-FRAP is depicted in Figure 3. The light source of the microscope was a 1064 nm

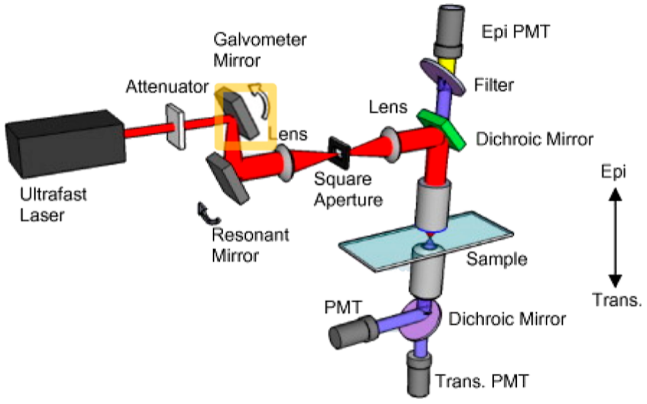

Figure 3. Instrument design for comb-bleach photobleaching: beam scanning is performed using a galvanometer (slow axis) and a resonant mirror (fast axis). Comb bleach patterns were produced by modulating power and changing the scan pattern of the galvanometer mirror (yellow box). PMT = photomultiplier tube.

near-IR femtosecond laser (Fianium FemtoPower; 150 fs pulses at 50 MHz repetition rate and up to 1 W average power at 1064 nm emission), passed through a second harmonic generation crystal to produce a frequency-doubled visible 532 nm beam. The laser beam was scanned across the sample using a galvanometer/resonant mirror pair with an 8.8 kHz resonant scanning mirror (Electro-optical Products Corporation, Ridgewood, NY) for the fast-scan axis and a galvanometer mirror (Cambridge-Tech, Bedford, MA) for the slow-scan axis. The mirror pair was 4f-coupled to the back of a 20×, 0.45 NA objective (Nikon, Melville, NY) to enable beam-scanning imaging at the focal plane.[35,36] For an incident wavelength of 532 nm, the diffraction-limited beam waist of ~700 nm was significantly smaller than the ~2 μm width of a pixel, such that resolution was likely to be limited by digitization. Each pixel in the FoV was measured sequentially as the laser beam was raster-scanned across the sample. Videos were recorded at approximately 2 frames per second.

Generation of the periodically structured photobleach pattern was performed through straightforward changes only to the slow-scan galvanometer mirror. Details are provided in the Supporting Information SI.V. Images from FT-FRAP experiments were analyzed using image processing software written in-house (MATLAB) and available on GitHub (https://github.itap.purdue.edu/Simpson-Laboratory-for-Nonlinear-Optics/FT_FRAP). Initial image segmentation was performed with the Fiji plugin: Trainable Weka Segmentation. Details of implementation can be found in the Supporting Information.

RESULTS AND DISCUSSION

Prior to analysis of the experimental measurements, the proposed FT-FRAP approach for segmented domain analysis was critically evaluated using simulations with known ground truth diffusivities and exchange rates. The results of simulations for samples with discrete boundaries between regions of different diffusivities are shown in Figure 4. All domains were generated from segmentation of fluorescence images acquired experimentally for ritonavir/PVPVA thin films. All simulations of diffusion and diffusion/exchange were performed exclusively in real-space by iterative convolution with a preset digital filter, as described in the Materials and Methods section, while all analyses of the segmented domains were performed exclusively in the spatial FT domain. Simulation ground truth values were selected to be within 1×10^{-3} to 1×10^{-2}, which span the range of experimental results. In all simulations, independently and identically distributed Gaussian noise of 2% was added to each pixel in the simulated time-traces prior to fitting. Error bars represent the root mean squared errors (RMSE) based on the deviations between the recovered decay coefficients and the true ground truth results used in the simulations. In the case of normal diffusion within monolithic domains described in Figure 2A, segmentation followed by subsequent analysis of the segmented domains yielded recovered diffusion coefficients in good agreement with the ground-truth values used in the simulations (within 5%). Similarly, good agreement was observed in the modeling of exchange-dominated kinetics, in which the real-space images were convolved with a filter consisting of an impulse combined with a low-amplitude Gaussian, collectively modeling exchange followed by comparatively fast interfacial diffusion. Recovered parameters from fits of the simulation results for exchange-dominated recovery were also within 5% of the ground truth. When allowing a combination of both exchange and diffusion using eq 3 in Supporting Information, parameters recovered from simultaneous fits of multiple harmonics of the simulations were within 10% of the ground truth. In contrast, fits of a single harmonic to recover exchange and diffusion parameters were ill-posed, effectively fitting one equation to two unknowns. Consistent with the theoretical predictions in eq 11, the recovery curves were insensitive to the particular form of the PSF used for photobleaching. Changes in the PSF (e.g., from astigmatism or "top-hat" photobleach profiles) affected the initial amplitudes of each spatial harmonic in the FT-domain. However, the locations of the harmonics (and the corresponding distance over which recoveries were evaluated) were dictated solely by the period of the bleach pattern and were independent of the PSF. It is worth emphasizing this distinct advantage of structured illumination relative to point-bleach FRAP measure-

https://doi.org/10.1021/acs.analchem.2c02950
Anal. Chem. 2023, 95, 2192−2202

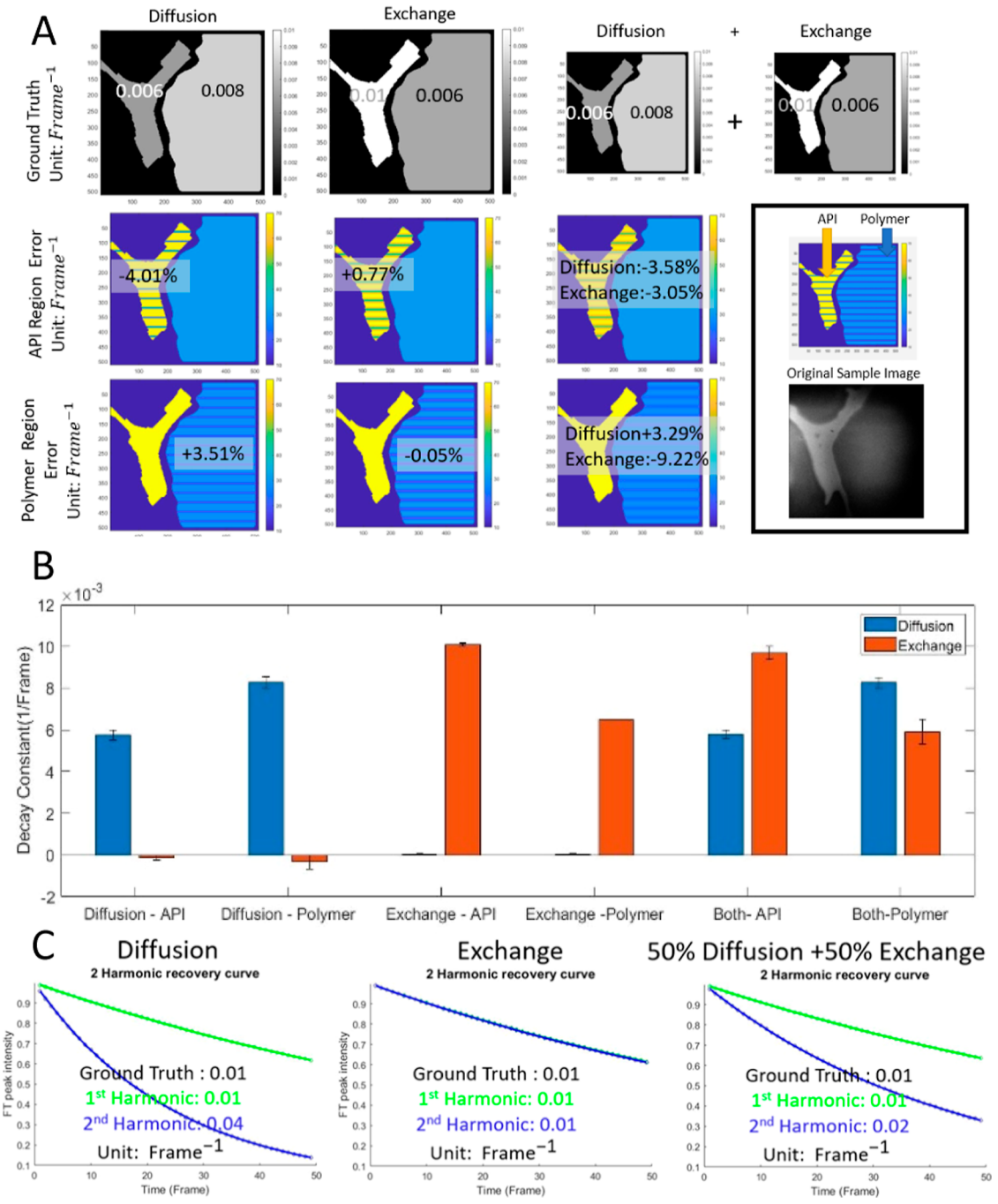

Figure 4. (A) Representative simulations of diffusion and exchange recovery with ground truth values shown in top images, with error bars indicating RMSE. (B) Recovered values for diffusion and exchange decay constants. (C) First two harmonics fits for both models.

ments, in which reliable characterization of the PSF is critical for quantitative analysis.[14]

These collective simulation results support the potential utility of FT-FRAP diffusion analysis within segmented domains of arbitrary shape. Furthermore, simulations suggest viability of the FT-FRAP approach for sensitively quantifying departures from normal diffusion through the integration of results at multiple harmonics. Simulations performed for FRAP recovery by normal diffusion, by exchange, and by combinations of both diffusion and exchanges yielded reliable recovery of the key mobility parameters, even in simulations performed exhibiting both diffusion and exchange in multiple domains with recovery times differing by over an order of magnitude within a single FoV.

Molecular diffusivities within thin films containing only the API (ritonavir) and a fluorescent reporter or only the polymer (PVPVA) and the reporter were measured to provide a baseline for interpretation of subsequent analyses of mixtures. For both media, measurements were performed using Nile red (NR) dye. Pure components results are shown in Figure 5. A summary of the results of the fits and error analysis is given in Table 1 for pure PVPVA thin films, with complementary results for ritonavir and mixtures in the Supporting Information. The total measurement uncertainty was decomposed into contributions from the FT-FRAP measurement

https://doi.org/10.1021/acs.analchem.2c02950
Anal. Chem. 2023, 95, 2192−2202

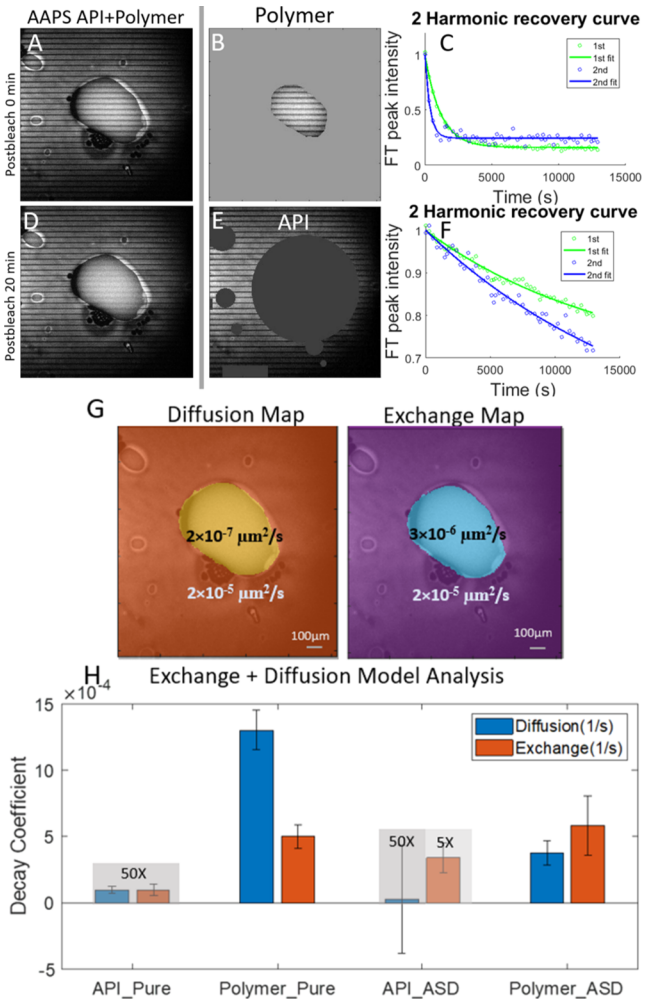

Figure 5. FT-FRAP results on pure API (ritonavir), pure polymer (PVPVA), and AAPS (amorphous/amorphous phase-separated) API/polymer ASD. (A,D) FT-FTAP recovery image at 0 and 20 minutes after the photobleaching. (B,E) FT-FRAP recovery images segmented for polymer (B) and API (E) domains. (C,F) Recovery curves for the first two harmonics for segmented polymer (C) and API (F) domains. (G) Recovered diffusion/exchange map from multiple segments (H) diffusion analysis results for FT-FRAP (diffusion + exchange model). Selected results were magnified to assist in visualization.

Table 1. Error Analysis for Pure PVPVA Sample

	decay coefficient (1/min)	propagated fit RSD σ_{fit} (%)	calculated sample RSD σ_{sample} (%)	total measured RSD σ_{total} (%)
k_{diff}	7.9×10^{-2}	2.3	10.9	11.1
k_{off}	3.0×10^{-2}	6.9	16.5	17.9

error and contributions from sample-to-sample variance across multiple fields of view. Uncertainties from the relative errors of the fits provided metrics dependent primarily on uncertainties arising within a single FoV and therefore reflect the inherent measurement error of FT-FRAP analysis (~2−7% RSD). This relative uncertainty was significantly lower than the total measurement uncertainty across multiple fields of view of ~11−18%, suggesting that the sample-to-sample variance across multiple fields of view dominated the relative uncertainty in the analysis. Assuming the total variance (σ_{total}^2) is given the sum of the measurement fit (σ_{fit}^2) and sample variance (σ_{sample}^2) consistent with the absence of covariance, the contribution from sample variance can be estimated by $\sigma_{sample}^2 = \sigma_{total}^2 - \sigma_{fit}^2$ and is included in Table 1 for comparison.

Diffusion accounted for in the Mittag−Leffler model include perturbations from distributions in step length (Lévy flight parameterized by μ) and distributions in dwell-times (parameterized by α, with $\alpha = 1$ corresponding to normal diffusion). For a glassy matrix of small molecules (ritonavir with trace water), the persistence length of structural heterogeneity within the matrix is unlikely to extend substantially over length scales greater than the dimensions of the comparably small fluorescent reporter. As such, neither mechanism for anomalous diffusion is reasonably expected within ritonavir spin-coated thin films.

While anomalous diffusion is not expected within thin ritonavir films based on structural arguments, previous studies have reported enhanced mobility at the interfaces of molecular glasses.[38,39] If one assumes that a high-mobility interfacial layer is in intimate contact with the bulk ritonavir consistent with these previous reports, recovery can arise either through diffusion within the bulk or through desorption from the bulk into the interfacial layer followed by exchange back to the bulk. If the mobility within the interfacial layer is fast relative to both bulk diffusion and the "on" rate for exchange back to the bulk, the recovery time is dominated in this limit by the "off" rate, corresponding to a discontinuous jump in diffusivity following desorption from the bulk to the interfacial layer. This model can be considered as a limiting case of Lévy flight for anomalous diffusion corresponding to μ approaching zero, for which the distribution in step lengths trends toward infinite steps. Consistent with the simulations depicted in Figure 2, recovery dominated by this exchange mechanism is expected to produce identical decay-time constants for all spatial harmonics in FT-FRAP, differing substantially from the distance-dependent recovery expected for diffusive motion. Leveraging the sensitivity of FT-FRAP with patterned illumination to deviations from anomalous diffusion allows quantification of the relative contributions of both exchange and diffusion within thin films.

Decomposing the spatially-dependent FRAP recovery into diffusive versus exchange contributions yields interesting trends in thin films of pure ritonavir and pure PVPVA at high humidity. Most notably, the recovery for pure ritonavir clearly includes significant contributions from exchange, consistent with the presence of an interfacial layer of higher mobility (exchange decay coefficient of $1.2 \pm 0.3 \times 10^{-4}$ min^{-1}, diffusion decay coefficient of $1.2 \pm 0.5 \times 10^{-4}$ min^{-1}, corresponding to a diffusion coefficient of $8.6 \pm 2.2 \times 10^{-8}$ $\mu m^2/s$). Mobility within PVPVA is two orders of magnitude faster than in the pure API, also containing significant contributions from both diffusion and exchange (exchange decay coefficient $3.0 \pm 0.5 \times 10^{-2}$ min^{-1}, diffusion decay coefficient $7.9 \pm 0.9 \times 10^{-3}$ min^{-1}, corresponding to a diffusion coefficient of $5.8 \pm 0.6 \times 10^{-5}$ $\mu m^2/s$).

These results for homogeneous pure thin films provide benchmarks for interpreting the recovery within phase-separated domains following high-humidity exposure of ritonavir/PVPVA mixtures. Following water vapor exposure, model ASD films comprised of ritonavir in PVPVA spontaneously produced heterogeneous domains, consistent with expectations for amorphous/amorphous phase separation. The Nile red fluorescent reporter exhibits increased quantum efficiency in hydrophobic domains likely to be dominated by

https://doi.org/10.1021/acs.analchem.2c02950
Anal. Chem. 2023, 95, 2192−2202

the API, suggesting the formation of API-rich "halos" around the droplet-shaped domains of high mobility, as shown in Figure 5. This trend was consistent across multiple different fields of view.

Recovery within the different segmented domains produced by phase separation evolved with radically different kinetics, with recovery arising over the time-course of 10's of minutes for the higher-mobility segmented domains and extending over several days in the lower-mobility segmented regions. Based on analogous mobility trends for the pure polymer and pure API films, the low mobility regions are attributed to API-rich phase-separated domains and the high mobility regions to polymer-rich domains.

The parameters recovered by multi-harmonic FT-FRAP kinetics analysis generally support these assignments. Specifically, the diffusion contribution to the mobility recovery in the slow-recovery domains is in good qualitative and quantitative agreement with the diffusion term observed in pure API films, consistent with assignment to phase separation to produce API-rich domains. Similarly, the exchange contribution in the high-mobility regions is within experimental uncertainty of the exchange term recovered for pure polymer films, suggesting similar kinetics for exchange to a higher-mobility interfacial layer. These results in combination with the overall magnitudes of the kinetics recovery support the assignment of the faster recovering phase-separated domains as polymer-rich and the slower recovering domains as API-rich.

Despite the qualitative and quantitative similarities in kinetics parameters associated with this assignment, the differences in kinetics in the phase-separated domains relative to the pure compounds are particularly intriguing. Most notably, the exchange term for the recovery within the API-rich domains was enhanced by 35-fold relative to thin films of pure API, greatly increasing the effective molecular mobility within the phase-separated API-rich domains. In addition, the diffusion term for the polymer-rich domains was reduced by nearly half, further increasing the relative importance of exchange-driven recovery within the polymer domains. These collective results suggest that consideration of interfacial mobility is clearly critical for quantitatively reliable modeling of molecular mobility within phase-separated ASD materials.

Given the dramatic increase in exchange-driven recovery within the API-rich phase-separated domains relative to the same API prepared as single-component thin films, it is tempting to forward hypotheses capable of accounting for the increased mobility. The presence of a substantial polymer contribution within the API-rich domains could potentially reduce the viscosity and increase molecular mobility. Phase separation will still generally result in an equilibrium concentration of polymer within the API-rich domain and API within the polymer-rich regions. The corresponding reduction in viscosity associated with incorporation of a hydrophilic polymer at high RH could potentially reduce viscosity and increase mobility. However, that mechanism would be expected to preferentially impact the diffusion component of the recovery. In practice, the diffusion rate within the API-rich domains changed minimally relative to the pure compound, with the greatest change arising in the exchange term. For this reason, we excluded reduction in bulk viscosity within the API-rich domains as a mechanism for the enhancement of recovery.[40]

Enhancement of the exchange contribution suggests a contributing role of the polymer in promoting interfacial exchange and diffusion within the API-rich domains. Given the hydrophilic nature of the glass substrate, vertical phase separation normal to the interface could potentially result in the presence of a polymer-rich interfacial layer bridging the substrate and the API-rich domains, depicted graphically in Figure 2 (not to scale). If present, such a hydrophilic interfacial layer could provide a conduit for fast diffusion following exchange, given the much faster diffusivity observed within the polymer-rich domains relative to API-dominated regions.

X-ray photoelectron spectroscopy (XPS) measurements were performed to quantify the exposed fraction of API and polymer following phase separation to test this hypothesis. For films prepared from 30% API by weight, the XPS results indicated surface exposure of 50% API, demonstrating a preferential partitioning of API at the exposed thin film interface. These observations are consistent with the hypothesized presence of a polymer-rich hydrophilic underlayer of high mobility at the glass interface in intimate contact with the API-rich domains.

These collective results have the potential to profoundly impact the manner in which dissolution is modeled and interpreted in design and optimization of pharmaceutical formulations. In ASD formulations exhibiting amorphous/amorphous phase separation, the kinetics associated with molecular mobility within the API-rich phase-separated domains have the potential to include significant and potentially dominant contributions from interfacial exchange in addition to bulk diffusion. In such instances, the interfacial surface area of the API-rich domains in combination with the intrinsic desorption rate may dominate the overall API dissolution kinetics, rather than the dissolution rate of the polymeric material. Depending on the desorption rate k_{off}, phase separation to produce API-rich domains could potentially result in dramatic reductions in dissolution kinetics. Such qualitative predictions are consistent with prior reports, in which the API dissolution rates were found to drastically *decrease* at high drug loadings, attributed to phase separation.[41]

The results presented in this work provide a framework for integrating structured illumination with FRAP to recover spatially resolved diffusivity maps, laying a foundation for extension to studies of molecular mobility within other heterogeneous assemblies. Previous measurements have shown the compatibility of comb-bleach FT-FRAP measurements with two-photon excitation,[15] suggesting compatibility with measurements through turbid media, including biological tissue. As turbidity is a hallmark of structural heterogeneity, extension of FT-FRAP with periodically structured illumination to probe diffusivity within systems exhibiting 3D heterogeneity is a potentially exciting avenue of future research.

The approach developed in this work has the potential to be easily retrofit into conventional beam-scanning confocal and multi-photon excited fluorescence microscopes. Most beam-scanning systems, including the Formulatrix system used in the present study, consist of a pairing of fast-scan and slow-scan mirrors to perform line-by-line imaging. If the galvo driver firmware is directly accessible (e.g., by the vendor), simple changes to reduce the number of slow-scan steps enable the comb-bleach patterns used in the present study. Even without access to the vender-controlled firmware as in the present study, re-routing the voltage normally delivered to the galvanometer mirrors is still reasonably straightforward. In either case, no changes in the physical hardware used for beam-

https://doi.org/10.1021/acs.analchem.2c02950
Anal. Chem. 2023, 95, 2192−2202

scanning imaging are necessary in order to retrofit instrumentation for FT-FRAP analysis to support diffusion mapping.

CONCLUSIONS

Diffusion imaging by FT-FRAP was theorized and demonstrated experimentally as a method for mapping diffusivity variability across an entire FoV, with sensitivity to quantitatively recover contributions arising from both bulk and interfacial diffusion. Diffusion maps were generated by encoding information in the spatial frequency domain through periodically patterned photoexcitation. The local contribution to each spatial frequency harmonic was obtained through image segmentation and spatial Fourier transformation. Analysis over the different length scales probed at different spatial frequency harmonics provided sensitive discrimination between bulk diffusion and recovery from exchange followed by interfacial diffusion. Diffusion imaging by FT-FRAP was validated using homogeneous and heterogeneous model systems for normal and anomalous diffusion. Quantitation of diffusion within phase-separated domains of ASDs revealed an important role of interfacial diffusion, which dominated mobility within the API-rich phase-separated domains. The dominant role of interfacial diffusion within these model assemblies suggests that kinetics models developed to describe dissolution trends in the design of ASDs may not yield predictive outcomes unless interfacial processes are integrated into the modeling.

ASSOCIATED CONTENT

Supporting Information

The Supporting Information is available free of charge at https://pubs.acs.org/doi/10.1021/acs.analchem.2c02950.

FT-FRAP measurements for pure polymer and API thin films; simulation methods and masks; evaluation of the influence of intra-domain diffusion heterogeneity; evaluation of surface enrichment of the ASD sample; illustration of the slow-scan beam pattern during imaging and periodic photobleaching; implementing diffusion + exchange diffusion modeling; and table of error analysis for pure API, ASD−API, ASD−polymer sample (PDF)

AUTHOR INFORMATION

Corresponding Author

Garth J. Simpson − *Department of Chemistry, Purdue University, West Lafayette, Indiana 47907, United States;* orcid.org/0000-0002-3932-848X; Email: gsimpson@purdue.edu

Authors

Ziyi Cao − *Department of Chemistry, Purdue University, West Lafayette, Indiana 47907, United States*

Dustin M. Harmon − *Department of Chemistry, Purdue University, West Lafayette, Indiana 47907, United States*

Ruochen Yang − *Department of Industrial and Physical Pharmacy, Purdue University, West Lafayette, Indiana 47907, United States*

Aleksandr Razumtcev − *Department of Chemistry, Purdue University, West Lafayette, Indiana 47907, United States;* orcid.org/0000-0001-9591-8612

Minghe Li − *Department of Chemistry, Purdue University, West Lafayette, Indiana 47907, United States*

Mark S. Carlsen − *Department of Chemistry, Purdue University, West Lafayette, Indiana 47907, United States*

Andreas C. Geiger − *Department of Chemistry, Purdue University, West Lafayette, Indiana 47907, United States;* Present Address: Undersea Sensor Systems Inc. 4868 E Park 30 Dr, Columbia City, IN 46725; orcid.org/0000-0002-0472-6648

Dmitry Zemlyanov − *Birck Nanotechnology Center, Purdue University, West Lafayette, Indiana 47907, United States;* orcid.org/0000-0002-1221-9195

Alex M. Sherman − *Department of Chemistry, Purdue University, West Lafayette, Indiana 47907, United States*

Nita Takanti − *Department of Chemistry, Purdue University, West Lafayette, Indiana 47907, United States;* Present Address: Thermo Fisher Scientific, 168 Third Avenue Waltham, MA USA 02451.

Jiayue Rong − *Department of Chemistry, Purdue University, West Lafayette, Indiana 47907, United States*

Yechan Hwang − *Department of Chemistry, Purdue University, West Lafayette, Indiana 47907, United States*

Lynne S. Taylor − *Department of Industrial and Physical Pharmacy, Purdue University, West Lafayette, Indiana 47907, United States;* orcid.org/0000-0002-4568-6021

Complete contact information is available at: https://pubs.acs.org/10.1021/acs.analchem.2c02950

Author Contributions

The manuscript was written through contributions of all authors. All authors have given approval to the final version of the manuscript.

Notes

The authors declare no competing financial interest.

ACKNOWLEDGMENTS

The authors gratefully acknowledge funding for the present work from Eli Lilly & Company and from the National Science Foundation through an NSF award (CHE-2004046) and from the NSF Center for Bioanalytic Metrology (IIP-1916691).

REFERENCES

(1) Elkhabaz, A.; Sarkar, S.; Simpson, G. J.; Taylor, L. S. *Pharm. Res.* **2019**, *36*, 174.

(2) Maincent, J.; Williams, R. O. *Drug Delivery Transl. Res.* **2018**, *8*, 1714−1725.

(3) Vasconcelos, T.; Marques, S.; das Neves, J.; Sarmento, B. *Adv. Drug Delivery Rev.* **2016**, *100*, 85−101.

(4) Buron, J. D.; Pizzocchero, F.; Jepsen, P. U.; Petersen, D. H.; Caridad, J. M.; Jessen, B. S.; Booth, T. J.; Bøggild, P. *Sci. Rep.* **2015**, *5*, 12305.

(5) Williams, S. P.; Haggie, P. M.; Brindle, K. M. *Biophys. J.* **1997**, *72*, 490−498.

(6) Lorén, N.; Hagman, J.; Jonasson, J. K.; Deschout, H.; Bernin, D.; Cella-Zanacchi, F.; Diaspro, A.; McNally, J. G.; Ameloot, M.; Smisdom, N.; Nydén, M.; Hermansson, A. M.; Rudemo, M.; Braeckmans, K. *Q. Rev. Biophys.* **2015**, *48*, 323−387.

(7) Meyvis, T. K. L.; De Smedt, S. C.; Van Oostveldt, P.; Demeester, J. *Pharm. Res.* **1999**, *16*, 1153−1162.

(8) Beaudouin, J.; Mommer, M. S.; Bock, H. G.; Eils, R.Experiment setups and parameter estimation in fluorescence recovery after photobleaching experiments: a review of current practice. *Model Based Parameter Estimation*; Springer, 2013; pp 157−169.

(9) Peters, R.; Peters, J.; Tews, K. H.; Bähr, W. *Biochim. Biophys. Acta, Biomembr.* **1974**, *367*, 282−294.
(10) Babinchak, W. M.; Surewicz, W. K. *Bio-Protoc.* **2020**, *10*, No. e3489.
(11) Offeddu, G. S.; Mohee, L.; Cameron, R. E. *J. Mater. Sci.: Mater. Med.* **2020**, *31*, 46.
(12) Hashlamoun, K.; Abusara, Z.; Ramirez-Torres, A.; Grillo, A.; Herzog, W.; Federico, S. *Biomech. Model. Mechanobiol.* **2020**, *19*, 2397.
(13) Lorén, N.; Nydén, M.; Hermansson, A.-M. *Adv. Colloid Interface Sci.* **2009**, *150*, 5−15.
(14) Mazza, D.; Cella, F.; Vicidomini, G.; Krol, S.; Diaspro, A. *Appl. Opt.* **2007**, *46*, 7401−7411.
(15) Geiger, A. C.; Smith, C. J.; Takanti, N.; Harmon, D. M.; Carlsen, M. S.; Simpson, G. J. *Biophys. J.* **2020**, *119*, 737−748.
(16) Robbins, G. P.; Jimbo, M.; Swift, J.; Therien, M. J.; Hammer, D. A.; Dmochowski, I. J. *J. Am. Chem. Soc.* **2009**, *131*, 3872−3874.
(17) Braeckmans, K.; Stubbe, B. G.; Remaut, K.; Demeester, J.; De Smedt, S. C. *J. Biomed. Opt.* **2006**, *11*, 044013.
(18) Wiesmeijer, K.; Molenaar, C.; Bekeer, I.; Tanke, H. J.; Dirks, R. W. *J. Struct. Biol.* **2002**, *140*, 180−188.
(19) Wehrle-Haller, B.Analysis of integrin dynamics by fluorescence recovery after photobleaching. *Adhesion Protein Protocols*; Springer, 2007; pp 173−201.
(20) Stavreva, D. A.; McNally, J. G. *Methods Enzymol.* **2004**, *375*, 443−455.
(21) Hagen, G. M.; Caarls, W.; Lidke, K. A.; De Vries, A. H. B.; Fritsch, C.; Barisas, B. G.; Arndt-Jovin, D. J.; Jovin, T. M. *Microsc. Res. Tech.* **2009**, *72*, 431−440.
(22) Braeckmans, K.; Peeters, L.; Sanders, N. N.; De Smedt, S. C.; Demeester, J. *Biophys. J.* **2003**, *85*, 2240−2252.
(23) Braeckmans, K.; Remaut, K.; Vandenbroucke, R. E.; Lucas, B.; De Smedt, S. C.; Demeester, J. *Biophys. J.* **2007**, *92*, 2172−2183.
(24) Davis, S. K.; Bardeen, C. J. *Rev. Sci. Instrum.* **2002**, *73*, 2128−2135.
(25) Smith, B. A.; McConnell, H. M. *Proc. Natl. Acad. Sci. U.S.A.* **1978**, *75*, 2759−2763.
(26) Davoust, J.; Devaux, P. F.; Leger, L. *EMBO J.* **1982**, *1*, 1233−1238.
(27) Blumenthal, D.; Goldstien, L.; Edidin, M.; Gheber, L. A. *Sci. Rep.* **2015**, *5*, 11655.
(28) Hobson, C. M.; O'Brien, E. T.; Falvo, M. R.; Superfine, R. *Biophys. J.* **2020**, *119*, 514−524.
(29) Liu, B.; Hobson, C. M.; Pimenta, F. M.; Nelsen, E.; Hsiao, J.; O'Brien, T.; Falvo, M. R.; Hahn, K. M.; Superfine, R. *Opt. Express* **2019**, *27*, 19950−19972.
(30) Rumondor, A. C.; Wikström, H.; Van Eerdenbrugh, B.; Taylor, L. S. *AAPS PharmSciTech* **2011**, *12*, 1209−1219.
(31) Li, M. H.; Razumtcev, A.; Yang, R. C.; Liu, Y. L.; Rong, J. Y.; Geiger, A. C.; Blanchard, R.; Pfluegl, C.; Taylor, L. S.; Simpson, G. J. *J. Am. Chem. Soc.* **2021**, *143*, 10809−10815.
(32) Indulkar, A. S.; Lou, X.; Zhang, G. G. Z.; Taylor, L. S. *Mol. Pharm.* **2019**, *16*, 1327−1339.
(33) Purohit, H. S.; Taylor, L. S. *Pharm. Res.* **2017**, *34*, 2842−2861.
(34) Metzler, R.; Klafter, J. *Phys. Rep.* **2000**, *339*, 1−77.
(35) Alford, W. J.; VanderNeut, R. D.; Zaleckas, V. J. *Proc. IEEE* **1982**, *70*, 641−651.
(36) Paddock, S. W. *Biotechniques* **1999**, *27*, 992−1004.
(37) Sarkar, S.; Song, Z.; Griffin, S. R.; Takanti, N.; Vogt, A. D.; Ruggles, A.; Danzer, G. D.; Simpson, G. J. *Mol. Pharm.* **2020**, *17*, 769−776.
(38) Wu, T.; Yu, L. *Pharm. Res.* **2006**, *23*, 2350−2355.
(39) Wu, T.; Sun, Y.; Li, N.; de Villiers, M. M.; Yu, L. *Langmuir* **2007**, *23*, 5148−5153.
(40) Yang, R.; Zhang, G. G. Z.; Kjoller, K.; Dillon, E.; Purohit, H. S.; Taylor, L. S. *Int. J. Pharm.* **2022**, *619*, 121708.
(41) Saboo, S.; Moseson, D. E.; Kestur, U. S.; Taylor, L. S. *Eur. J. Pharm. Sci.* **2020**, *155*, 105514.

https://doi.org/10.1021/acs.analchem.2c02950
Anal. Chem. 2023, 95, 2192−2202